Biochimica et Biophysica Acta 1830 (2013) 5014–5026

Contents lists available at SciVerse ScienceDirect

Biochimica et Biophysica Acta

journal homepage: www.elsevier.com/locate/bbagen

Manipulating the bioactivity of hydroxyapatite nano-rods structured networks: Effects on mineral coating morphology and growth kinetic ☆

Noelia L. D'Elía [a], A. Noel Gravina [a], Juan M. Ruso [b], Juan A. Laiuppa [c], Graciela E. Santillán [c], Paula V. Messina [a,*]

[a] Department of Chemistry, Universidad Nacional del Sur, INQUISUR-CONICET, (8000) Bahía Blanca, Argentina
[b] Soft Matter and Molecular Biophysics Group, Department of Applied Physics, University of Santiago de Compostela, Santiago de Compostela 15782, Spain
[c] Department of Biology, Biochemistry and Pharmacy, Universidad Nacional del Sur, (8000) Bahía Blanca, Argentina

ARTICLE INFO

Article history:
Received 18 March 2013
Received in revised form 25 June 2013
Accepted 19 July 2013
Available online 25 July 2013

Keywords:
Hydroxyapatite
Trabecular bone
Bioactivity
Nano-rods
Sol–gel method
Osteoblast viability

ABSTRACT

Background: Nano-hydroxyapatite particles have better bioactivity than the coarse crystals. So, they can be utilized for engineered tissue implants with improved efficiency over other materials. The development of materials with specific bioactive characteristics is still under investigation.
Methods: The surface properties of four hydroxyapatite materials templated by different micelle-polymer structured network are studied. The synergistic interaction of each block copolymer in contact with CTAB rod-like micelles results in crystalline HAp nano-rods of 25–50 nm length organized in hierarchical structures with different micro-rough characteristics.
Results: It was observed that the material in vitro bioactivity strongly depends on the surface structure while in a minor extent on their Ca/P ratio. So, MIII and MIV materials with Skewness parameter $R_{sk} > 2.62$ favored the formation on their surfaces of net-like phase with a high growth kinetic constant; while MI and MII ($R_{sk} \leq 2.62$) induced the appearance of spherulitic-like structures and a growth rate 1.75 times inferior. Material biocompatibility was confirmed by interaction with rat calvarial osteoblasts.
Conclusions: The different structures growth is attributed to a dissimilar matching of crystal planes in the material and the apatite layer formed. In specific synthesis conditions, a biocompatible material with a Ca/P ratio close to that for the trabecular bone and a morphology that are considered essential for bone-bonding was obtained.
General significance: The creation of implantable devices with a specific bioactive characteristic may be useful to manipulate the attachment of cells on mineral coating directly affecting the stability and life of the implant. This article is part of a Special Issue entitled: Protein trafficking & Secretion.

© 2013 Elsevier B.V. All rights reserved.

1. Introduction

Synthetic hydroxyapatite (HAp, $Ca_{10}(PO_4)_6(OH)$) has a chemical similarity to the inorganic component of bone matrix and exhibits strong affinity to host hard tissues [1]. The most significant advantages of synthetic HAp are its biocompatibility, slow degradation in situ, and good osteoconductive/osteoinductive capabilities [1,2] making it an ideal candidate for the construction of orthopedic and dental implantable devices. Synthetic HAp has been widely used in bone repair, bone augmentation, as well as in coatings of metal implants or acting as a filler in bone or teeth [3,4]. However, the low mechanical strength of typical HAp ceramics, especially in a wet environment, generally restricts its use in low load-bearing applications [5]. Recent advances in nanoscience and nanotechnology have added new attention to the development of nanosized HAp materials and the study of their properties at the nanoscale. Current applications of nano-HAp include surface modifications of HAp to modulate their colloid stability [6–8], prevent dissolution in the case of low pH to avoid inflammation and as an intermediate layer to allow strong bond formation between HAp-polymer matrices. HAp nanoparticles have also served as non-viral carriers for drug delivery and gene therapy because of their recognized biocompatibility, ease of handling and well-known adsorption affinity [9–13]. Furthermore, HAp nanoparticles can be stably loaded with radioisotopes [11]. After loading with genes or drugs by adsorption, HAp nanoparticles provide a protective environment that shields them from degradation while providing a convenient pathway for cell membrane penetration and the controlled release of the gene/drug [12]. The research results indicate the potential of nano-HAp in gene delivery and as drug carriers [12,13] Nanocrystalline HAp powders exhibit sinterability and enhanced densification due to their greater surface area, which may improve fracture toughness as well as other mechanical properties [14]. Moreover, nano-HAp, compared to coarse crystals is expected to have better bioactivity. Thus, nano-HAp particles can be utilized for engineered tissue implants with improved bioactivity over other materials [1].

In consideration of its multiple applications and even when many HAp materials with multiform morphologies were prepared by a variety of techniques [15–19]; it is of great importance to develop new nano-HAp synthesis methods focused on the precise control of

☆ This article is part of a Special Issue entitled: Protein trafficking & Secretion.

* Corresponding author. Tel.: +54 291 4595159; fax: +54 291 4595160.
E-mail address: pmessina@uns.edu.ar (P.V. Messina).

0304-4165/$ – see front matter © 2013 Elsevier B.V. All rights reserved.
http://dx.doi.org/10.1016/j.bbagen.2013.07.020

particle size morphology and chemical composition. Bio-inspired by bio-mineralization, morphogenesis has been emerging as an important environmentally friendly route to generate inorganic materials with controlled morphologies by using self-assembled organic superstructures, inorganic or organic additives, and/or templates with complex functionalization patterns [20]. As an alternative strategy, using water soluble polymers as crystal modifiers for controlled crystallization is widely increasing and becomes a benign route for controlling and designing multiple inorganic architectures. These additives do not act as supramolecular templates which predefine the latter hybrid material structure, but usually act as a soluble species at various hierarchy levels of the forming mineral hybrid similarly to what occurs in nature.

Here we present a study that involves different hexadecyltrimethylammonium bromide (CTAB) micelles–block copolymer organized networks to create bioactive superstructures resulting from HAp nano-rods associations. At the synthesis conditions CTAB forms rod-like micelles of 47 nm length [21] that template the deposition of PO_4^{-3} and Ca^{2+} ions favoring the formation of bone dimensioned HAp nano-rods. The interaction with block copolymers restrings the crystals' growth and directs their association inducing the final structure arrangement. The structure set-up and evolution relies on a synergistic effect of the mutual interactions of the confined reaction media environment (block copolymer network) in contact with the external template (CTAB rod-like micelles). The manipulation of such interactions permits the alteration of the chemical and/or the surface properties on the synthesized materials and their subsequent bioactivity, including mineral coating morphology and growth kinetic. The proposed method lets us obtain bioactive and biocompatible materials which may allow us to replicate to some extent the bone structure, HAp nanorods of 25–50 nm length organized in hierarchical structures. Such characteristics are desirable to reproduce in a synthetic material thinking of its future use as nanoscopic building units of tissue engineered scaffolds designed to mimic the structural and biological functions of native extracellular matrix (ECM).

2. Experimental

2.1. Materials

Hexadecyl-trimethyl ammonium bromide (CTAB, MW = 364.48 g mol^{-1}, 99% Sigma), poly(ethylene glycol) 400 (PEG 400, Sigma-Aldrich, MW = 380–420 g mol^{-1}, δ = 1.126 g cm^{-3} at 25 °C), poly (propylene glycol) (PPG, Sigma-Aldrich, MW = 425 g mol^{-1}, δ = 1.004 g cm^{-3} at 25 °C), Poly(ethylene glycol)-block-poly(propylene glycol)-block-poly(ethylene glycol) (PEG–PPG–PEG, PEG 10 wt.%, Sigma-Aldrich, MW = 2800 g mol^{-1}, δ = 1.018 g cm^{-3}), Octylphenyl-polyethylene glycol (IGEPAL® CA 630, $(C_2H_4O)_nC_{14}H_{22}O$, Sigma-Aldrich, MW = 603 g mol^{-1}, δ = 1.06 g cm^{-3} at 25 °C), sodium phosphate (Na_3PO_4, MW = 148 g mol^{-1}, 96% Sigma), calcium chloride ($CaCl_2$, MW = 91 g mol^{-1}, 99% Sigma) and sodium nitrite ($NaNO_2$, MW = 69 g mol^{-1}, 97%) were used without further purification (as a reference their structures are shown in Scheme 1). For solution preparation, only triple-distilled water was used.

2.2. HAp material synthesis

Four materials (denoted as I, II, III and IV) were prepared using a modification of the method proposed by Liu et al. [22]; descriptions of the selected synthesis condition are shown in the electronic supplementary material (ESM). Material I: first, 350 mL of a 3.13 mM CTAB aqueous solution was mixed with 20 mL of PPG and stirred at 500 rpm for 10 min. Second, 200 mL of 2 M sodium nitrite aqueous solution and 2.2 g calcium chloride were incorporated in sequence. Finally, 200 mL of 0.14 M of Na_3PO_4 aqueous solution was added to the above mixed solution drop by drop at room temperature under magnetic stirring at 500 rpm. Finally 20 mL of 2 M sodium nitrite aqueous solution and 0.22 g calcium chloride were incorporated in sequence. After the integration of all reactants, the solution was magnetically stirred for 1 h. The resulting gels were left for 24 h in an autoclave at 100 °C. The obtained materials were filtered, washed with triple-distilled water to remove impurities. Finally, the surfactant was completely removed by acidic solvent extraction technique [23,24].

For samples II, III and IV the preparation protocol was similar to that described for sample I with the exception of 20 mL of PEG, PEG–PPG–PEG and IGEPAL® CA 630 respectively instead of PPG.

2.3. Field emission scanning electron microscopy (FE-SEM)

Surface morphology was evaluated using a field emission scanning electron microscope (FE-SEM ZEISS UTRA PLUS). To acquire all the SEM images a Secondary Electron Detector (in lens) was used. The accelerating voltage (EHT) applied was 3.00 kV with a resolution (WD) of 2.1 nm. Local compensation of charge (by injecting nitrogen gas) or the sample shading was not necessary. The associated energy-dispersive spectrophotometer provided qualitative information about surface elemental composition. The topography of samples was quantified from SEM microphotographs using different software packages [25], uncertainty of 5%.

2.4. Transmission electron microscopy (TEM)

Transmission electron microscopy was performed using a Philips CM-12 transmission electron microscope equipped with a digital camera MEGA VIEW-II DOCU and operated at 120 kV with magnification of 730,000×. Observations were made in a bright field. Powdered samples were placed on copper supports of 2000 mesh. High resolution transmission (H-TEM) microphotographs were taken using a Libra 200 FE OMEGA transmission electron microscope operated at 200 kV with magnification of 100,0000×. Observations were made in a bright field. Powdered samples were placed on carbon supports of 2000 mesh.

2.5. X-ray powder diffraction

Powder X-ray diffraction (XRD) data were collected with a Philips PW 1710 diffractometer with Cu K_α radiation (λ = 1.5418 nm) and Graphite monochromator operated at 45 kV; 30 mA and 25 °C. The mean crystalline size (δ) of the particles was calculated from XRD line broadening measurement using the Scherrer equation [26]:

$$\delta = \frac{0.89\lambda}{\beta \cos\theta} \tag{1}$$

where λ is the wavelength (Cu K_α), $\beta$is the full width at the half maximum of the HAp (211) line and θ is the diffraction angle. The fraction of crystalline phase (X_c) of HAp powders was evaluated by the following equation [26]:

$$X_c = \frac{1-\upsilon_{112/300}}{I_{300}} \tag{2}$$

where I_{300} is the intensity of (300) diffraction peak and $\upsilon_{112/300}$ is the intensity of the hollow between (112) and (300) diffraction peaks of HAp. The estimated uncertainties are about 20%.

2.6. FT-IR spectroscopy

The experiments were done in a Nicolet FT-IR Nexus 470 Spectrophotometer. To avoid co-adsorbed water, the samples were dried under vacuum until constant weight was achieved and diluted with KBr powder before the FT-IR spectra were recorded.

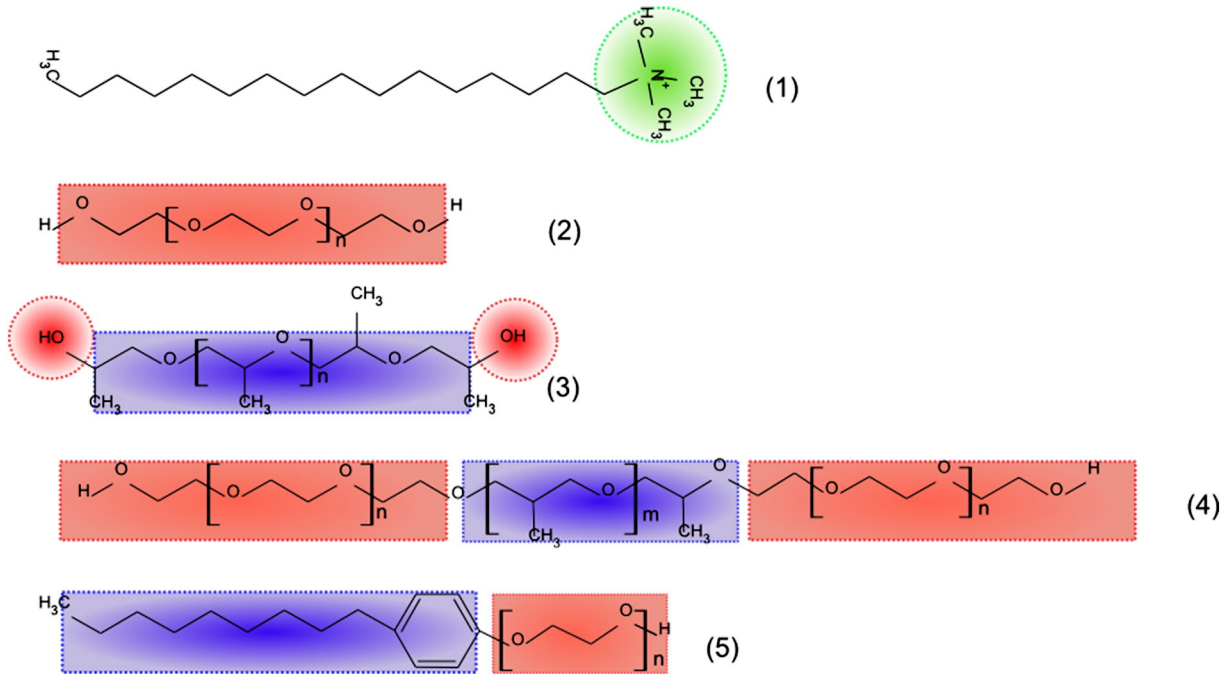

Scheme 1. Molecular structure of: (1) hexadecyl-trimethyl ammonium bromide (CTAB), (2) poly(ethylene glycol) 400 (PEG 400), (3) poly(propylene glycol) (PPG), (4) poly(ethylene glycol)-block-poly(propylene glycol)-block-poly(ethylene glycol) (PEG–PPG–PEG) and (5) octylphenyl-polyethylene glycol (IGEPAL® CA 630).

2.7. Zeta potential (ζ) measurements

A Malvern Zeta Sizer Nano (ZS90) with a He-Ne laser (λ = 633 nm) was used for Zeta potential (ζ) measurements. Malvern's software provides the zeta potential from electrophoretic mobilities (μ_E), using the Henry equation [27].

2.8. NMR spectroscopy

Spectra were recorded at frequencies of 300 MHz and 121 MHz for ^{1}H and ^{31}P respectively in a Bruker spectrophotometer after 128 scans. The material samples were dispersed in deuterated water (1% p/v), sonicated for 120 min to obtain a stable suspension.

2.9. Bioactivity assay

To perform the bioactivity assay, the material was kept in contact with simulated body fluid (SBF) following the standard procedure described by Kokubo et al. [28], which has a composition and ionic concentration similar to that of human plasma, containing Na^{+} (142.0 mM), K^{+} (5.0 mM), Mg^{2+} (1.5 mM), Ca^{2+} (2.5 mM), Cl^{-} (148.8 mM), HCO^{3-} (4.2 mM), HPO_4^{-2} (1.0 mM) and SO_4^{-2} (0.5 mM). The synthesized materials were soaked in 1.5 SBF at 37 °C for periods of 1, 3, 6, 10, 15, 20, 30, 65 days, the specimens were removed from fluid, rinsed with distilled water and dried. The temperature (37 °C) was maintained by placing the samples in a thermostated bath throughout the experiment.

2.10. Osteoblast isolation

Calvarial osteoblasts were obtained from 5-day-old neonatal rats which were sacrificed by fast decapitation. All procedures were carried out in conformity with the Guide for the Care and Use of Laboratory Animals published by the US National Institutes of Health (NIH Publication No. 85-23, revised 1996). Briefly, calvarias were incubated in PBS containing 4 mM EDTA at 37 °C for two 10-min periods, and the supernatants were discarded. Subsequently, calvarias were rinsed in PBS and submitted to digestion in PBS containing 200 U/ml collagenase for four 15-min periods. Cells released during the first digestion were discarded, and those released during the subsequent digestions were spun down, collected and combined after centrifugation for 10 min at 1500 rpm. Then, cells were cultured at 37 °C in α-MEM supplemented with 15% FBS, 1% penicillin and streptomycin under humidified air (5.5% CO_2). After 24 h, the medium was replaced by α-MEM supplemented with 10% PBS, 1% penicillin and streptomycin, and the cells were cultured until ~80% of confluence (2–3 days). Then, the cells were frozen in liquid nitrogen until their use.

2.11. Osteoblast culture and treatment

Treatments were performed in two ways: T1) Calvarial osteoblasts were seeded in 48-well plates in the presence or the absence of the nano-particles (50 μg/well) and then cultured for 48 and 72 h in α-MEM supplemented with 10% FBS, in a humidified atmosphere (5.5% CO_2) at 37 °C. T2) Calvarial osteoblasts seeded in 48-well plates were cultured for 1 day in α-MEM supplemented with 10% FBS, in a humidified atmosphere (5.5% CO_2) at 37 °C. Then, 50 μg per well of nanoparticles were added to adhered cells and the incubation continued for 48 and 72 h. After treatments, the cells were observed and microscopic photographs were taken by a Nikon Eclipse TE 300 microscope coupled to a Nikon Digital Sight DS U2 camera.

2.12. Cell viability and statistical analysis

After experiments, the controls and treated cells with the nanoparticles were washed with PBS buffer and stained with 0.1% of Trypan Blue dye as previously described [29]. The samples were then observed in an inverted microscope. Cells were counted per field and the percent of cells that excluded the stain (viable cells) with respect to the total cells (viable + non-viable cells) was obtained. Statistical significance of data was evaluated using Student's *t*-test and probability values below 0.01 ($P < 0.01$) were considered highly significant [30]. Quantitative data are expressed as means ± standard deviation (SD) from the indicated set of experiments. To evaluate the cell morphology in the

presence of the materials, the samples were then smeared on a microscope slide, air dried, fixed with absolute ethanol and stained by Giemsa stain [31].

3. Results and discussion

3.1. HAp nano-rods

3.1.1. Microstructure, morphology and topology characterization

3.1.1.1. Physical characteristics. Fig. 1 shows the SEM microphotograph of HAp powders obtained from CTAB/PPG, CTAB/PEG, CTAB/PEG–PPG–PEG and CTAB/IGEPAL® CA 630 template system after 24 h of hydrothermal treatment. As can be seen, all obtained materials present the aspect of nano-structured networks. The samples were diluted in ethanol, sonicated and inspected by transmission electron microscopy (TEM), Fig. 2, and it can be observed that each of them is composed of uniform rod-like particles with similar aspect ratios (length/diameter). Size distribution histograms are shown in ESM. Without the polymer addition, the obtained material is formed by elongated (70–150 nm length and 15–20 nm diameter) and separated crystals larger than CTAB micelles [21] in agreements with literature findings [5,32,33], ESM. The mechanism by which each polymer interacts with CTAB micelles and determines the final material characteristics will be evaluated afterward; but in general we may say that the presence of the polymer molecules causes the reduction of nano-HAp particle size to 7–9 nm diameter and 25–50 nm length.

The topography of each material surface is characterized typically by a succession of peaks and valleys, which can be quantified using either 2D profiles or 3D parameters. In order to evaluate the sample surface profiles, the surface roughness was analyzed. Using digitalized scanning electron microscopy (SEM) images, Fig. 1, and different software packages [25], we computed the roughness arithmetical average deviation (R_a); the root mean square roughness (R_q), maximum height of peaks (R_p), maximum depth of valleys (R_v), maximum height of the profile (R_t), Kurtosis (R_{ku}) and Skewness (R_{sw}) coefficients. Each parameter is described below.

The arithmetic average height parameter (R_a), also known as the center line average (CLA), is the most universally used roughness parameter for general quality control. It is defined as the average absolute deviation of the roughness irregularities from the mean line over sampling length as shown in Fig. 3a. The mathematical definition and the digital implementation of the arithmetic average height parameter are, respectively, as follows [34].

$$R_a = \frac{1}{n}\int_0^l |y(x)|dx \tag{3}$$

$$R_a = \frac{1}{n}\sum_{i=1}^{n}|y_i|. \tag{4}$$

To represent the standard deviation of the surface height distribution, the root mean square roughness (R_q) was used. It is an important parameter to describe the surface roughness by statistical method. This parameter is more sensitive than the arithmetic average height (R_a) to a large deviation from the mean line. The mathematical definition and the digital implementation are as follows [34]:

$$R_q = \sqrt{\frac{1}{l}\int_0^l \{y(x)\}^2 dx} \tag{5}$$

$$R_q = \sqrt{\frac{1}{n}\sum_{i=1}^{n} y_i^2}. \tag{6}$$

The R_q mean line is the line that divides the profile so that the sum of the squares of the deviations of the profile height from it is equal to zero.

Maximum height of peaks (R_p) and maximum depth of valleys (R_v) are defined as the maximum height and the maximum depth of the profile above and below the mean line within the assessed length. The

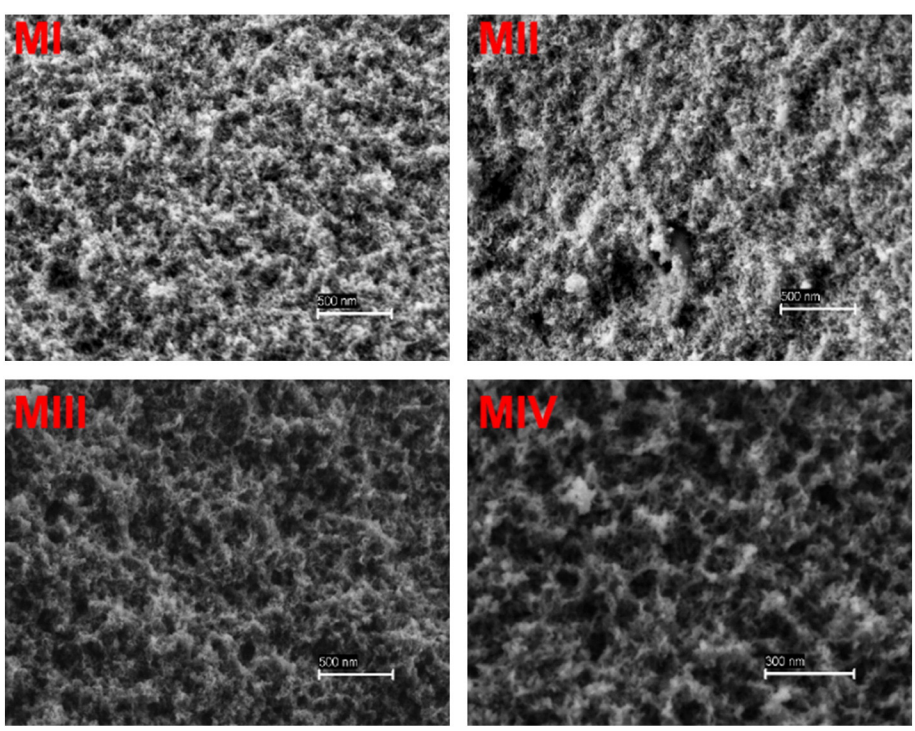

Fig. 1. SEM microphotographs of HAp materials.

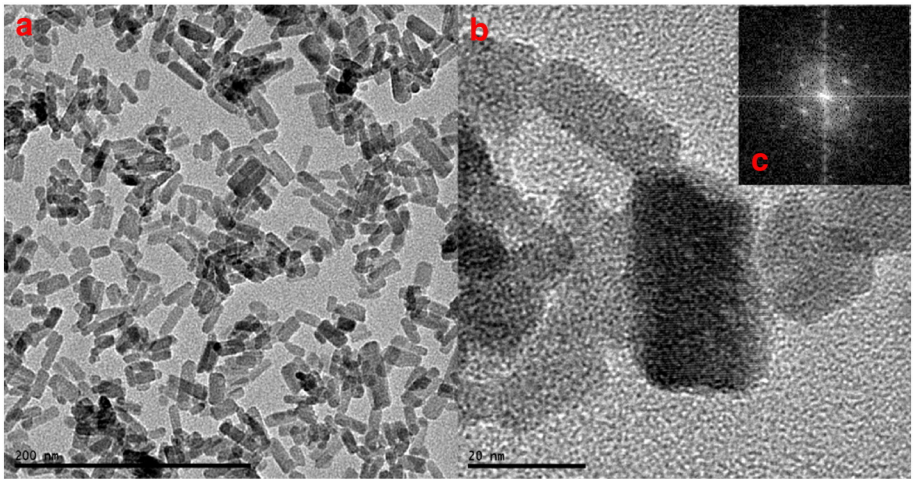

Fig. 2. TEM and H-TEM microphotographs of HAp nano-rods, sample MIII. (a) HAp nano-rods, (b) crystalline planes of HAp nano-rods, (c) selected-area electron diffraction (SAED) patterns of HAp nano-rods.

relationship between them is defined as maximum height of the profile (R_t)

$$R_p = \max_i y_i \tag{7}$$

$$R_v = \min_i y_i \tag{8}$$

$$R_t = R_p - R_v. \tag{9}$$

To measure the symmetry of the roughness profile about the mean line, the profile skewness was analyzed. This parameter is sensitive to occasional deep valleys or high peaks. A symmetrical height distribution, i.e. with identical peaks as valleys, has zero skewness. Profile with peaks removed or deep scratches have negative skewness. Profiles with valleys filled in or high peaks have positive skewness. Skewness parameter (R_{sk}) can be used to distinguish between two profiles having the same R_a or R_q values but with different shapes. The mathematical and the numerical formula used to calculate the skewness of a profile, which has a number N of points, are as follows:

$$R_{sk} = \frac{1}{R_q^{\,3}} \int_{-\infty}^{\infty} y^3 p(y) dy \tag{10}$$

$$R_{sk} = \frac{1}{N R_q^{\,3}} \left(\sum_{i=1}^{N} Y_i^{\,3} \right) \tag{11}$$

where Y_i is the height of the profile at point number i.

Kurtosis coefficient (R_{ku}) describes the sharpness of the profile probability density. If $R_{ku} < 3$ the distribution curve is said to be platykurtoic and has relatively few high peaks and low valleys. If $R_{ku} > 3$ the distribution curve is said to be leptokurtoic and has relatively many high peaks and low valleys. The kurtosis parameter can also be used to differentiate between surfaces, which have different shapes and the same value of R_a.

$$R_{ku} = \frac{1}{R_q^{\,4}} \int_{-\infty}^{\infty} y^4 p(y) dy \tag{12}$$

$$R_{ku} = \frac{1}{N R_q^{\,4}} \left(\sum_{i=1}^{N} Y_i^{\,4} \right). \tag{13}$$

The fractal architecture should also be assessed, since this concept is particularly interesting in surface and material science. Natural fractals are repetitive patterns that are self-similar across a finite range of scales and many biological structures, including bone, are fractal or even fractal-like. Its influence and relevance on biological tissue is unknown, but implant surfaces might reveal this type of repetitive patterns at the micro-, nano- and crystal scales during quantitative morphology. To compute fractal dimension (D_f), the box counting method was applied to different SEM images. This protocol was used in a previous work [35] and consists of applying an increasingly fine grid over the area studied and counting, at each iteration, the number of boxes containing at least one part of the object to be measured. The fractal dimension Df is then linked to the number $n(s)$ of boxes of dimension s necessary to fill the surface area of the particle according to [36]:

$$D_f = \lim_{s \to 0} \frac{\ln n(s)}{\ln(1/s)}. \tag{14}$$

This method was also optimized by means of a calculation procedure stemming from the work of Foroutan-Pour et al. [37] which allows a precise determination of key parameters of the method, namely the number and the dimensions of the boxes [38]. The images, initially with 256 gray levels and 1024 × 768 pixels in size, are converted to

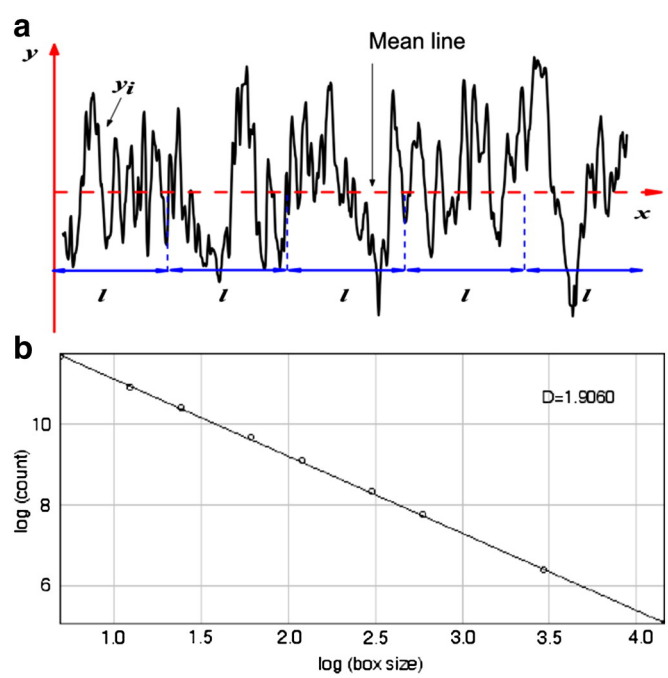

Fig. 3. (a) Schematic representation of the arithmetic average height parameter (R_a) for sample MIII. (b) Log of box size vs. the log of the pixel count.

Table 1
Chemical and physical characteristic of HAp materials.

	Polymer	CTAB/pol.[a]	Ca/P	δ/nm	X_c	D_{2D}	D_{3D}	R_q/nm	R_a/nm	R_{sk}/nm	R_{ku}/nm	R_p/nm	R_v/nm	R_t/nm
MI	PPG	1/43	1.97	20	75	1.832	2.641	174.85	119.75	1.45	2.12	255	300	−5
MII	PEG	1/51	1.92	34	85	1.855	2.652	167.11	109.40	1.52	2.32	275	356	−81
MIII	PEG–PPG–PEG	1/7	1.62	28	80	1.868	2.657	157.35	97.03	1.61	2.62	128	256	−128
MIV	IGEPAL	1/32	2.03	40	67	1.906	2.676	141.53	78.56	1.78	3.24	123	340	−217

[a] Molar ratio.

binary images. The fractal dimension is then derived from the slope of a least-square linear fit of the plot of *log n versus log* (*box size*), where *n* is the number of non-overlapping equal boxes that would fill the projected surface area of the aggregate. This operation can be carried out by different software packages [25], Log–log representations of the calculations of fractal dimension on the systems studied are shown in Fig. 3b.

Most authors, based on the Minkowski–Bouligand dimension and the content of projections on the directions of planes, have demonstrated that, in general, there is no general relationship between 3D and 2D fractal dimensions [39]. However, functional relationships between 2D and 3D fractal dimensions were found for specific systems, such as aluminum oxide nanoparticles, [40] assuming a uniform mass distribution of the object along the third dimension:

$$D_{3D} = 0.47D_{2D} + 1.78. \quad (15)$$

Obtained results are summarized in Table 1. It can be seen that a decrease in the R_q and R_a values and an augment of fractal dimension occurs from MI to MIV materials. The five highest peaks and five deepest valleys averaged over the total surface are given by R_q; it is therefore, always bigger than the equivalent R_a measured for the same area. The R_{sk} and R_{ku} indicate the asymmetry of the surface; all materials present positive values of R_{sk} denoting the presence of profiles with filled valleys and/or high peaks. The relationship between the number of peaks and valleys is given by the value of R_{ku}; MI, MII and MIII materials are platykurtoic and have relatively few high peaks and low valleys, while MIV is leptokurtoic and has relatively many high peaks and low valleys.

A relationship can be established between the topographical parameters and the polymers used during the template process, specifically to the length and the number of polyoxyethylene chains (PEG) present. MIII and MIV materials prepared using diblock copolymers PEG–PPG–PEG and IGEPAL® CA 630 showed the smoothest surface while the MI and MII samples synthesized using the homo-polymers PPG and PEG had the most irregular topography. IGEPAL® CA 630 and PEG–PPG–PEG molecules possess both hydrophobic and hydrophilic moieties and they form mixed aggregates in the presence of CTAB [41]. The hydrophobic unit composed by an octylphenyl-chain (IGEPAL® CA 630) or a PPG block chain (PEG–PPG–PEG) were placed inside mixed CTAB aggregates while the hydrophilic one (a PEG chain with 7 EO units in the case of IGEPAL® CA 630 and two 3 EO units PEG chains for PEG–PPG–PEG) is located outside micelles in contact with water. The protruding parts of the polymers interact through hydrogen bond [42] linking aggregates in a kind of compact structured networks. In the case of the homo-polymers PPG and PEG, their chains are completely hydrophilic or hydrophobic and are totally outside or inside the aggregates except the two ends—OH groups located between the polar heads of CTAB. The aggregates' connection decrease, and also the structuring effect. Thus the PEG chain ability to bind the micelles in a dense arrangement is manifested in the final inorganic material topological properties as we analyzed below.

3.1.1.2. Chemical characteristics. The material microstructure was analyzed by X-ray diffraction (XRD) patterns; high resolution electron microscopy (H-TEM); energy dispersive X-ray (EDX) analysis, ζ-potential, Fourier transform infrared (FT-IR) and nuclear magnetic resonance (NMR) spectroscopy. All synthesized samples correspond to crystalline materials with all peaks that could be indexed to hexagonal HAp, Fig. 4. The wide peaks indicate the presence of HAp particles with very small size in agreement with TEM images, Fig. 2a and b. Microcrystalline structure was also evidenced by the evaluation of the selected-area electron diffraction (SAED) patterns that can be extracted from the Fourier transform (FFT) of high resolution TEM microphotographs by digitalized image processing. Several single-crystal spot electron diffraction (ED) images, as that reported in Fig. 2c were obtained. The ED representation displays a perfect hexagonal pattern, which can be indexed as from HAp [0 0 1] zone axis [43]. EDX patters analysis show a Ca/P ratio of about 1.92, 1.97, 1.62 and 2.04 for materials MI, MII, MIII and MIV respectively, ESM. Only the MIII material presents a Ca/P ratio value within the generally accepted range between 1.60 and 1.67 resembling to the stoichiometric HAp. The excess calcium observed in the other materials was assigned to $Ca(OH)_2$. The DRX of the samples after calcination at 650 °C (ESM) show the presence of CaO indicating that the synthesized powder should be constituted by a mixture of HAp and $Ca(OH)_2$ which is the stable form of CaO at room temperature (the reversible dehydroxylation of $Ca(OH)_2$ occurs around 400 °C [44]).

The electronic properties of HAp are sensible to many variables, such as preparation methods, defects, size of the nano-crystals, surface reaction with the atmosphere, etc. Therefore, to investigate the electronic structure, it is necessary to evaluate the atomic properties of the constituents in HAp material synthesized by a particular method. Fig. 5 shows the FT-IR spectra of sample MIII. The broad band observed at 1650 and 3440 cm^{-1} indicate adsorbed water in the materials. The material shows phosphate absorption bands at 1036 (ν_3), 602 (ν_2), 563 (ν_4) and 470 (δ) cm^{-1}. Intense bands appearing at wave number values of 1420 and 1480 cm^{-1} are indicative of the carbonate ion substitution just with a low intensity peak at 880 cm^{-1}. High intensity peaks at 3000–3700 cm^{-1} are due to the bending vibration peak of OH-groups. The analysis of FT-IR spectra indicates that calcium phosphate coatings are carbonate hydroxyapatites (CHAs), presumably a mixture of AB substitution type (A type: $CO_3^{2-} \rightarrow OH^-$ substitution and B type: $CO_3^{2-} \rightarrow PO_4^{3-}$ substitution) with a major proportion of type A substitution. From the analysis of 3000–3700 cm^{-1} region almost five peaks can be recognized related to the O – H stretch. The band at 3440 cm^{-1} corresponds to adsorbed water, the others at 3744, 3223, 3100 and 3000 cm^{-1} may be assigned to different structural OH groups in HAp crystals (−OH groups with more or less hydrogen bond association to phosphate groups, and others with less or no interactions with the environment). The ^1H NMR spectrum displayed two signals centered at 7 ppm and 14 ppm attributed to structural OH groups and the protons of hydrogen phosphate groups as in $CaHPO_4$ respectively; while the ^{31}P-RMN spectrum showed a broad peak centered at 3.4 ppm that corresponds to P in nano-crystalline HAp [45]. Furthermore, ζ-potential measurements showed a value of surface charge density of about −11 mV in agreement with the presence of negative −OH groups at the material exterior. Comparable results have been observed in a previous work [46].

3.1.2. Template-polymer networks

A bio-inspired morpho-synthesis has been used to generate HAp rod-like nano-crystals. The principle that controls crystallization and morphosynthesis in the presence of a micellar–polymer template

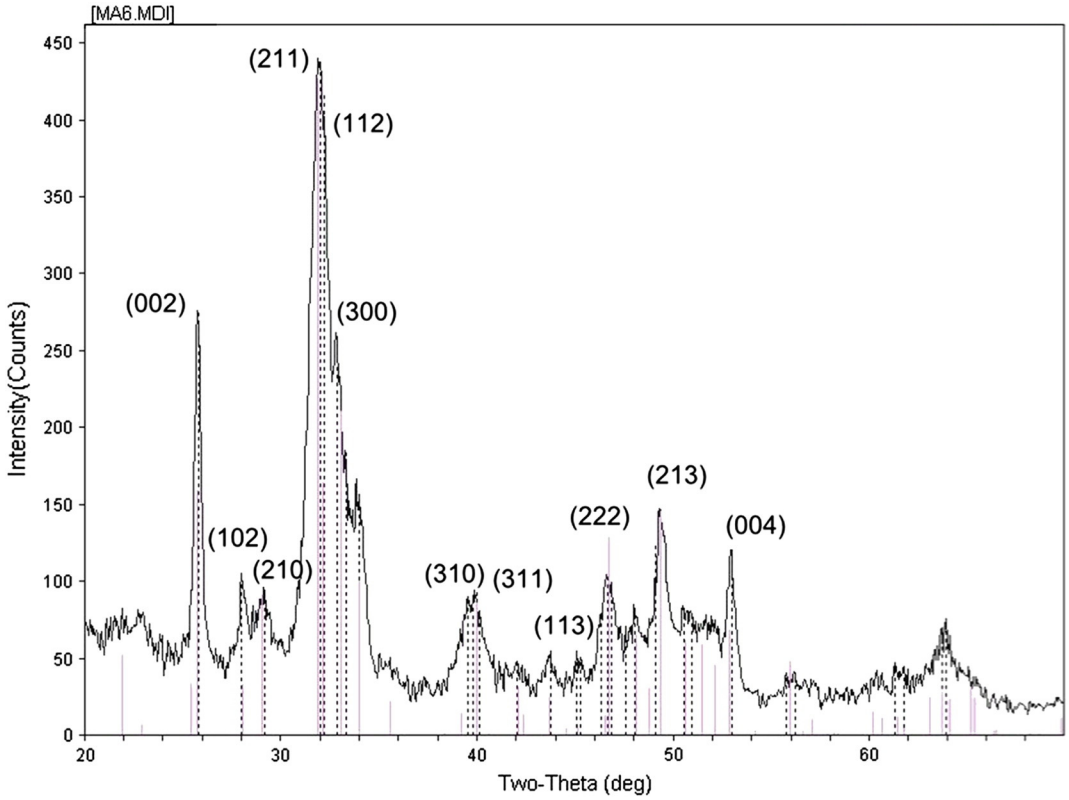

Fig. 4. XRD pattern of dried MIII without calcination. All peaks could be indexed to hexagonal HAp crystal (JCPDS 00-09-0432).

network implies both the transcriptive template effect provided by the presence of CTAB molecules in the rod-like micelles, and the synergistic effect of the mutual interactions between functionalities of the polymer and inorganic species. The CTAB/polymer systems and their interaction at the bulk solution have been studied widely by several researches [41,47]. Hydrophobic and less water soluble PPG molecules strongly interact with CTAB to form CTAB/PPG mixed micelles at a total solution concentration better than $(7.0–8.8) \times 10^{-4}$ M [41,48]. At the material synthesis conditions CTAB/PPG ~ 1/43, aggregates are typically composed of the polymer while CTAB molecules act as a good solvent for the polypropylene chains. In contrast, the hydrophilic homo-polymer PEG wraps around the CTAB micelle while most of the polymer molecules form loops in the surrounding water [41]. The presence of PEG molecules (CTAB/PEG ~ 1/51) increases the CTAB micellar critical concentration to 1.1×10^{-3} M [47]. The triblock co-polymers PEG–PPG–PEG and IGEPAL® CA 630 consist of water- and oil-soluble segments. It is well established that such polymers may bridge different domains of the same type [49] and can form aggregates in contact with water ($CMC_{IGEPAL} = 0.75 \times 10^{-4}$ M [50]). Also, both polymers form mixed aggregates in the synthesis conditions (CTAB/PEG–PPG–PEG ~ 1/7; CTAB/IGEPAL® CA 630 ~ 1/32 [50]). CTAB/IGEPAL® CA 630 and CTAB/PEG–PPG–PEG micelles show poly-oxy-ethylene chains protruding out from the aggregates, Scheme 2b. The presences of POG chains permit the creation of a necklace model among cross-linked block copolymer micelles [42,51]. Tasaki et al. [42,47] performed a Molecular Dynamic Simulation of PEG with 15 ethylene oxide (EO) units in aqueous solution to examine the hydration, the conformation of PEG, the water structure and the dynamics near PEG. Their investigation also revealed a rather complex hydration structure of PEG in water. A single molecule of water placed between every two EO units acts as a bridge between PEG chains. We think that a similar behavior occurred during the material synthesis, Scheme 2c. Tasaki et al. [42] also found the enhanced water structures near PEG at 100 °C, though they are less significant than those at 25 °C. These facts make us suppose that the polymer structural organization among CTAB micelles persists even through hydrothermal treatment and restricts the particle growth of the micellar surface. As a result, the length of HAp rods does not exceed 47 nm corresponding to the length of the cylindrical CTAB micelles [21]. At any moment bicontinuous structures are seen in the material, just an association of HAp rod-like nanoparticles, meaning that during the material formation the polymer mineralization has not taken place and the HAp deposition is restricted only to the micellar surface. However there is a change in the material crystalline structure and surface morphology according to the employed polymer. The ability of different polymers to interact with inorganic crystals as well as the fine-tuning of morphosynthesis properties is well recognized [20]. The anisotropic growth of the particles can be explained by the specific adsorption of additives to particular faces therefore, inhibiting the growth of these faces by lowering their surface energy [20]. Furthermore, whether the polymer just decorates single micelles or forms bridges between them, in both cases the intermicellar interaction potential will effectively be changed by the polymer chain. Such fact alters the distance between micelles and consequently, as we can see above, the material surface area and porosity.

The means by which mineralized tissues are achieved is not fully understood, but several authors have suggested that HAp crystals could be nucleated by a complex made of polyanionic proteins, probably a phosphoprotein [52]. In aqueous systems, CTAB would ionize completely and result in a cation with tetrahedral structure, Scheme 2a. Meanwhile, the phosphate anion has also a tetrahedral structure. So, the CTA^+ cation can interact favorably with the PO_4^{-3} anion complementing each other in a steric and in an electrostatic mode, Scheme 2a. Probably the PO_4^{-3} ions replace the Br^- in CTAB micelles and then attract Ca^{2+} in a process called "molecule recognition" [5] that could have taken place

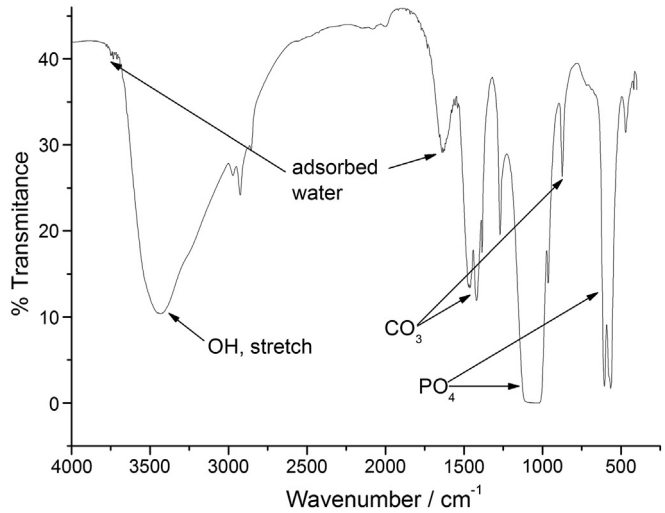

Fig. 5. FT-IR spectra of dried MIII as obtained.

at the template interface. The rod-like micelles thus act as nucleating points for the growth of HAp crystals presumably like native phosphoproteins in the mineralized tissue.

3.2. Bioactivity assays

3.2.1. Ca/P coating micromorphology

Osseo-integration is defined experimentally as the closest contact between bone and implant material in histological section and, in clinical terms, as the stability and ankylosis of an implant in bone. In consideration of osseo-integration concept the chemical and physical characteristics of the interface between bone and implant have a key role in accelerating bone healing and improving bone anchorage to the implant. A simpler method to estimate the bone-bonding potential of materials consists of the immersion of this material in simulated body fluid (SBF). According to Kokubo et al. [28,53], an essential requirement is the formation of a calcium phosphate layer on the material surface, usually called bone-like apatite. This bone-like apatite seems to activate signaling proteins and cells to start the cascade of events that results in bone formation [54]. In other words, a way to evaluate in vitro the in vivo behavior is from the bioactivity test by immersion of the synthetic material into SBF solution. In the bioactivity test, the biomimetic Ca/P deposition implies mimicking the natural process of mineralization without involving cellular and organic species. In this regard, the so called bioactive synthetic materials are materials that are able to nucleate and grow on them a layer of bone-like apatite in contact with SBF.

Fig. 6, shows the SEM microphotographs of apatite coatings deposited on the studied materials after 10 days incubation in 1.5 SBF. SEM images demonstrated that the above described chemical and physical material characteristics regulated the mineral coating micro-morphology. The role of surface texture in cell guidance is well known, but how this aspect affects bioactivity is still the subject of investigation [54]. All mineral coating formed on material surfaces were continuous layers, with differences in microscale morphologies. Mineral coating formed on MI material exhibited a spherulitic micro-morphology. The nuclei were spherical-like globules with 3–5 μm in diameter composed of agglomerates of plate-like nano-morphology crystals of ~150 nm length, Fig. 7a–c. It can be found that the ends of plate-like crystals are composed of

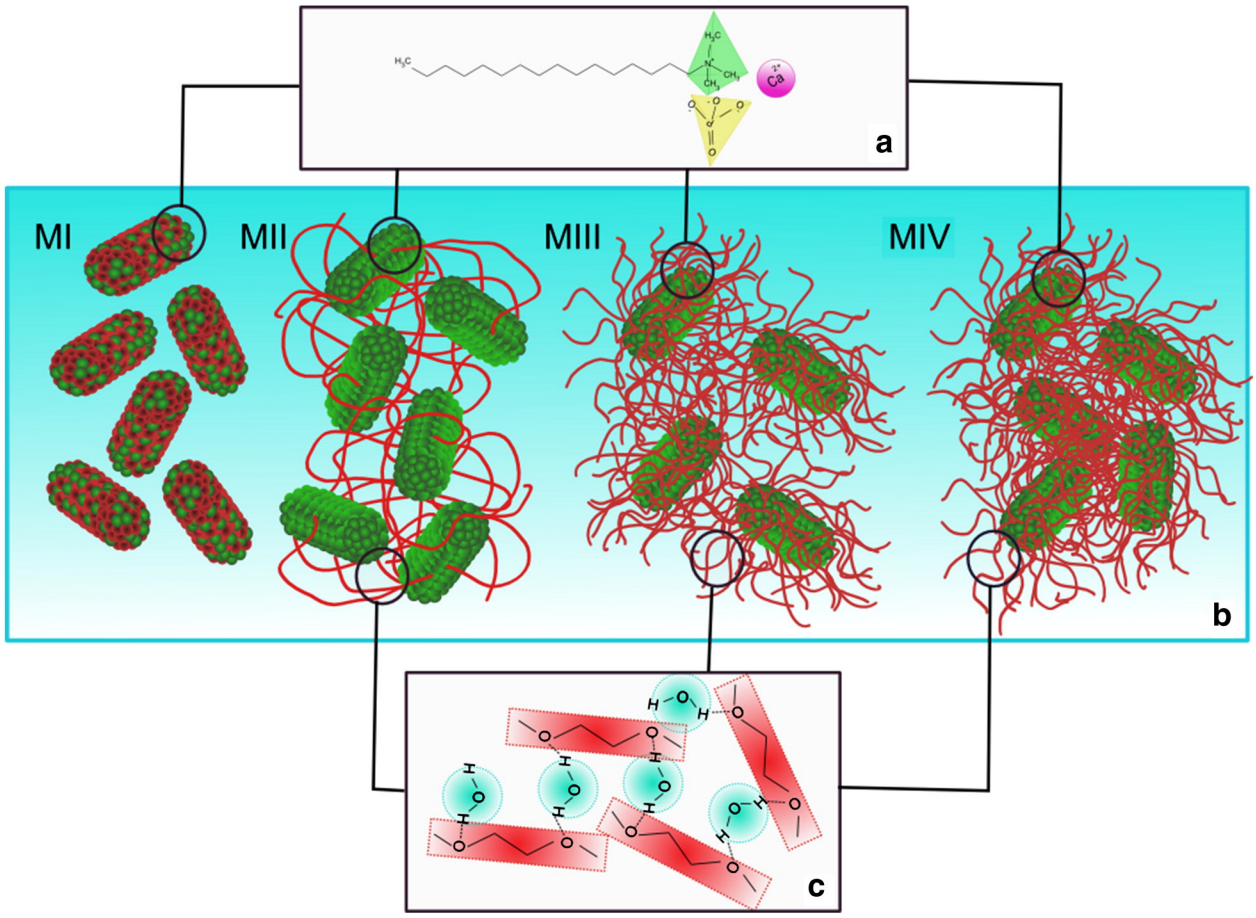

Scheme 2. Schematic representation of (a) ions CTA^{-}, PO_4^{-3} and Ca^{2+}; (b) polymer-CTAB micelles and (c) polymer chains interactions.

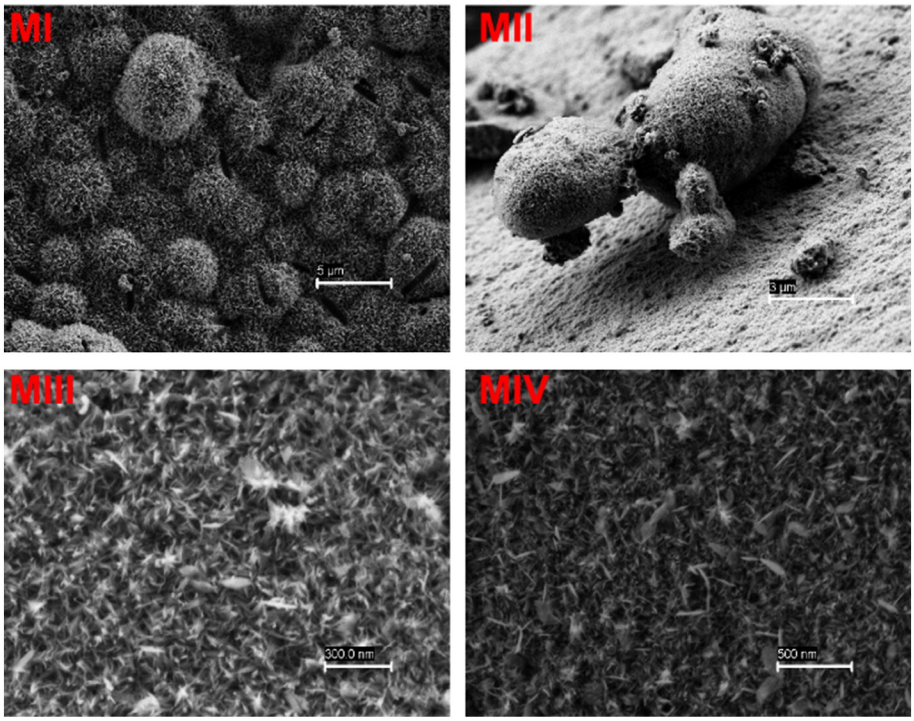

Fig. 6. SEM microphotographs of apatite coatings deposited on MI, MII, MIII and MIV materials after 10 days incubation in 1.5 SBF.

several nano-wires which are very smooth and straight, Fig. 7c. Spherulitic micro-morphology was transformed into net-like structures of about 60–100 nm length, Fig. 7b and d, by decreasing the material Ca/P ratio and surface roughness. So, coating deposited on MII showed a high proportion of net-like phase and some isolated spherulitic networks; whereas in the layers deposited on materials MIII and MIV the spherulitic morphology is completely absent. A similar dependence of deposited mineral coating morphology with Ca/P proportion was shown by Choi et al. [55] by modulating ion concentration in modified SBF during mineral nucleation and growth.

The morphology of mineral coating deposited on MIV has a similar aspect to that observed on MIII. The observed structures follow a direct relation with material surface roughness while not to a great extent with the Ca/P ratio variation. This fact led us to infer that in our materials, rugosity is the key factor to determine the coating deposition characteristics. On rough surfaces, the valleys seem to be the preferential sites for the nucleation and growth of calcium phosphates. Surfaces with positive (or less negative) skewness (R_{sk}) could favor Ca-rich phase deposition [54]. Although all synthesized materials presented high positive R_{sk} values; materials MIII and MIV showed $R_{sk} \geq 2.62$

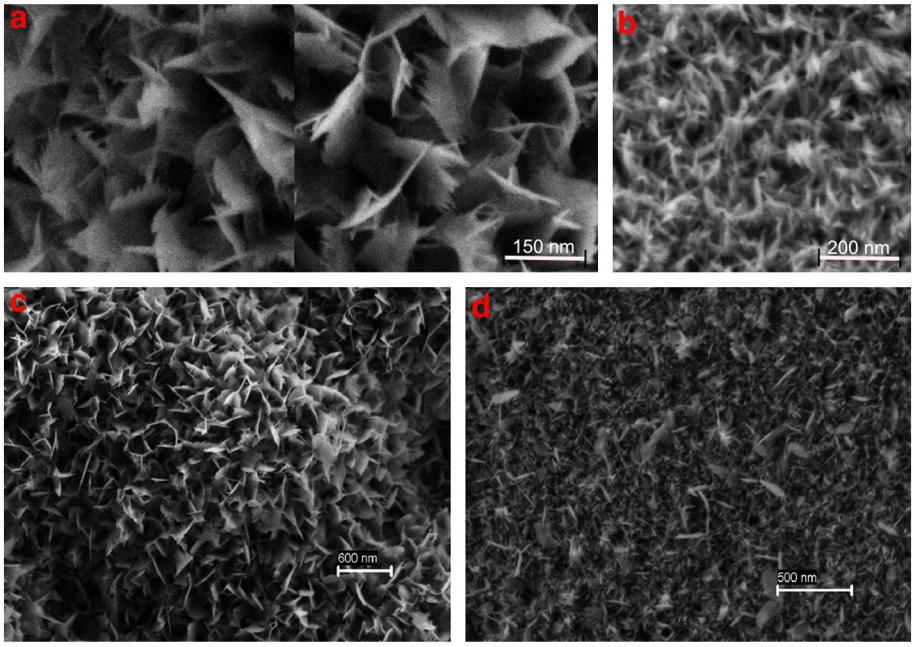

Fig. 7. SEM microphotographs of apatite coatings (a, c) spherulitic and (b, d) net-like micro-morphologies.

Table 2
Chemical and physical characteristics of Ca-P coatings on MI, MII, MIII and MIV materials.

	Coating micro-morphology	Ca/P	D_{2D}	D_{3D}	R_q/nm	R_a/nm	R_{sk}/nm	R_{ku}/nm
MI	Spherulitic-like	1.56	1.650	2.555	133.81	69.34	1.891	3.573
MII	Spherulitic-like; net-like	1.42	1.695	2.576	150.28	88.51	1.691	2.871
MIII	Net-like	1.03	1.763	2.608	170.03	113.26	1.493	2.241
MIV	Net-like	1.11	1.725	2.591	150.69	89.02	1.686	2.857

while MI and MII posses $R_{sk} \leq 2.32$. Differences in valleys deep would cause a dissimilar crystal nucleation and the manifestation of a singular morphology.

The coatings' morphological differences also provide diversity in their fractal dimensions, surface roughness and chemical composition. The surface roughness and fractal dimension of the mineral coatings with spherulitic-like micro-morphology was lower than net-like mineral coatings, Table 2. EDX microanalysis (ESM) showed that after the bioactivity assay the material with spherulitic-like coating showed a Ca/P = 1.56 that would be ascribed to deficient HAp crystals. The MI material and the Ca-P globules covering its surface exhibited a Ca/P ratio close to that for the trabecular bone [54] and their morphology are similar to that Kokubo et al. [56] consider essential for bone-bonding. The apatite present in the bone is calcium-deficient with dissolved carbonate, sodium and potassium ions and Ca/P ratio varying from 1.50 (trabecular bone) to 1.63 (cortical bone) [54]. Kokubo et al. [56] assume that the events involving osteoblasts occur only when a layer of similar composition and morphology to bone apatite is present on the implant surface. In addition, Wang et al. [57] considered titanium materials coated with a layer of carbonate apatite globules the most appropriated surface for cell attachment.

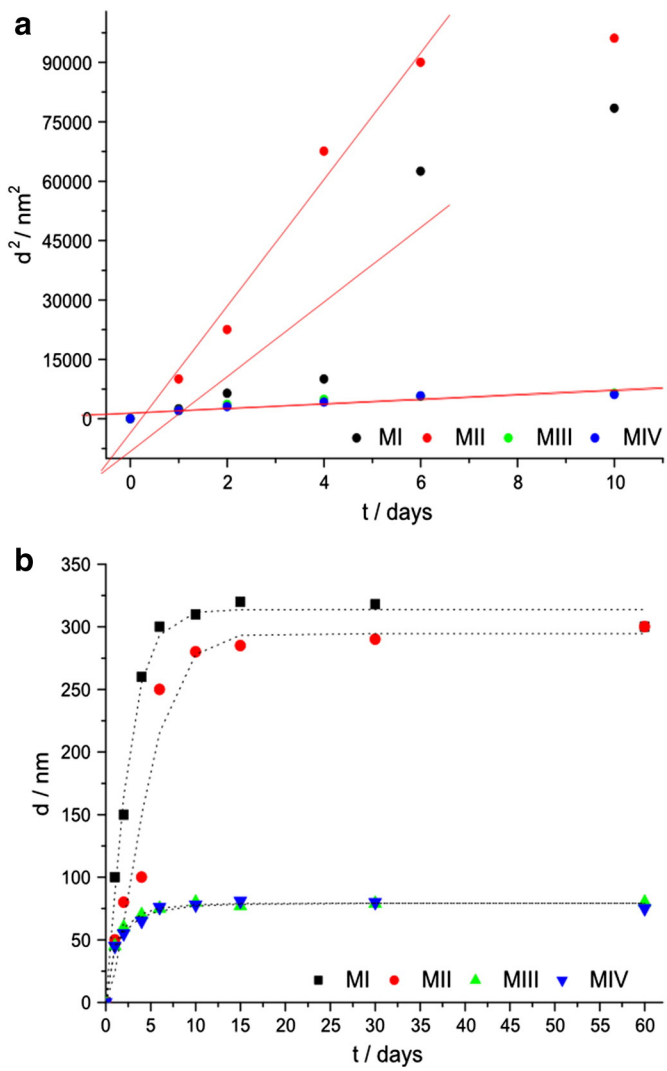

Fig. 8. Kinetic growth of apatite coatings on MI, MII, MIII and MIV materials. (a) Empirical (Eq. (16)) and (b) Avrami (Eq. (17)) equations.

The appearance of a net-like micro-morphology on materials surfaces is followed by a diminution of Ca/P ratio composition. The Ca/P ~ 1 presented by materials MIII and MIV covering with net-like micro-morphology layers is the typical value of the resorbable forms of calcium phosphates such as brushite (dicalcium phosphate dehydrate, Ca/P = 1) or octacalcium phosphate (Ca/P = 1) also present in the calcified tissues in a minor proportion [3].

3.2.2. Ca/P coating growth kinetic

Time evolution of apatite-like coating growth on the synthesized material was followed by SEM (ESM). The thickness of the apatite-like coating increases with time and reaches a saturated point after about 10 days of soaking for all materials. Assuming that the growth rate of apatite coating is controlled by the calcium and phosphorus ion diffusion rates from the SBF to the material surface, the growth kinetics of apatite-like coatings on porous materials can be expressed by an empirical relationship applied for the HAp growth on siliceous materials in a previous work [46]:

$$d^2 = kt \tag{16}$$

where d is the thickness of the coating evaluated from SEM photos, t is the soaking time for the biomimetic deposition and k is the growth rate constant. A plot of the square of the coating thickness (d^2) versus soaking time (t) is shown to be linear, Fig. 8a.

A deep analysis of crystals growth kinetic was performed by the application of Avrami equation:

$$d = d_{\max}\left(1 - \exp^{-(k_{Av} \times t)^n}\right) \tag{17}$$

where d_{max} is the maximum reached coating thickness, k_{Av} is the Avrami kinetic constant and n the reaction order. The modeling of the nucleation, growth and agglomeration of particles from a solution has been described for a number of various conditions in some details [58]. Most of these models are so intricate and include so many terms as to be intractable for many experiments. A much simplified version of these analysis is the Avrami equation [58]. This equation is derived using the general geometry of the growing precipitate and includes, to leading order, the effect of depletion of the parent phase during the reaction. As such, it provides a quantitative description of the kinetics of a transformation in a medium where the total amount of reactants is restricted, but is simple enough to be tractable for the analysis of most experimental data [59]. The growth kinetic of Ca/P layers on all tested materials is best described by the Avrami kinetic equation, Table 3. For those coatings composed of spherulitic or net-like pure phases, the equation fit to experimental data with a R^2 ~ 0.99. A less R^2 value (~0.96) was obtained for the application of Avrami equation to material MII coating, probably because it is composed of means of two different morphologies, each one with a distinct growth rate. Net-like coating phases that have a preferential growth on those materials with high proportion of deep valleys on theirs surfaces (MIII and MIV) present the highest values of kinetic constant with an $n < 1$; while for

Table 3
Growth kinetic parameters of Ca-P coatings on HAp materials.

	Coating micro-morphology		Avrami kinetic equation				Empirical equation	
		d_{exp}/nm	d_{max}/nm	k_{Av}/day^{-1}	n	R^2	K/nm^2day^{-1}	R^2
MI	Spherulitic-like	300	313 ± 5	0.39 ± 0.02	1.18 ± 0.11	0.994	15997 ± 108	0.990
MII	Spherulitic-like; net-like	250–300	294 ± 16	0.20 ± 0.03	1.53 ± 0.38	0.960	8742 ± 200	0.943
MIII	Net-like	75–80	79 ± 1	0.79 ± 0.04	0.70 ± 0.05	0.998	583 ± 125	0.899
MIV	Net-like	60–75	79 ± 2	0.70 ± 0.08	0.67 ± 0.10	0.991	573 ± 89	0.9146

spherulitic coating phases, the Avrami constant is 1.75 lower and the reaction order is superior to the unity.

With regard to the surface topography, the concentration of Ca and P ions were oversaturated and crystal nuclei were formed on the valleys of Ca/P materials. During this reaction, the materials themselves played the roles of Ca, P sources and ion retarded. The literature [60] indicates that Ca^{2+} and PO_4^{3-} ions gradually dissolve into distilled water to form $Ca_9(PO_4)_6$ clusters (namely Posner cluster: positively charged on the surface) which is considered to be the growth unit of HAp crystal. It is well known that hexagonal HAp crystals have two types of crystal surfaces with different charges, positive on *a*-surfaces and negative on *c*-surfaces. Usually, hexagonal HAp particles grow along the c-axis more easily since a strong bond site for $Ca_9(PO_4)_6$ clusters exists in the [0001] direction but no such site is present in $\left[10\bar{1}0\right]$ direction. In spherulitic-like phase's coatings, HAp grows in a radial way to construct each globule, and each nucleus becomes the center of one globule.

Materials MI, MII and MIV present higher Ca/P ratio values than MIII. According to Liu et al. [60], when additional Ca^{2+} ions were introduced into the reaction environment, they would attach to c-surfaces which were negatively charged. Thus there would be fewer Posner clusters incorporated onto *c*-surfaces. The growth of c-surfaces was less predominant leading to the aggregation of *a*- and *b*-planes and the growth of net-like phases. But in our case, if the Ca^{2+} ions were the inhibitors of c-surface growth, the structure variation could not be explained. Other scientists proposed that the epitaxial growth of apatite-like phases takes place by means of the matching of the structure of crystal planes in the material and the apatite layer formed [35]. The acceleration of the nucleation of apatite on material surfaces can have different causes, that is, because of (i) particle size, (ii) roughness or (iii) both particle size and roughness. Taking into account that the surface heterogeneity topographies of MI, MII, MIII and MIV materials have significant differences; the acceleration of the apatite nucleation on all surfaces is attributed to the surface topographical changes at the micrometer level.

3.2.3. Osteoblast-material interaction

The biocompatibility of materials was confirmed by assessing their interaction with neonatal rat calvarial osteoblasts; viability and cell adhesion were evaluated after 24, 48 and 72 h of treatment by microscopic observation. When osteoblasts were seeded in the presence of the material (T1), after 24 h they showed adherence to the culture plate in a similar manner to the control cells. In a second procedure the cells were plated and 24 h later the material was added (T2); in such conditions no significant changes were observed in the cell adhesion after 48 and 72 h of treatment compared with control and with T1, ESM. During the process of adhesion and spreading in the presence of material, the cell behavior was similar to control in both treatments; they showed their typical polygonal or widespread forms with fine filopodia and abundant surface folds, Fig. 9. No significant differences in cell viability after 72 h of both treatments (T1 and T2) with respect to the controls were observed (control: 94.21 ± 4.2%; T1: 97.62 ± 5.62%; T2: 98.72 ± 4.92%).

4. Conclusions

The results in this study indicate that controlling surface micro-rough properties is an efficient platform to manipulate the material bioactivity. Particularly, we used four crystalline HAp nano-rods structured materials created by different CTAB-micelle-block copolymer structured networks. In the specific synthesis conditions, CTAB would ionize completely and its interaction with PO_4^{-3} is steric and electrostatically favored. The ulterior Ca^{2+} attraction initiated the HAp crystal nucleation at the micelle interface. The presence of polymer and its structural organization among CTAB micelles restrict HAp growth to the micellar surface. As a result, the length of HAp rods does not exceed the 47 nm corresponding to the size of cylindrical CTAB micelles. The analysis of TEM microphotographs demonstrates that bicontinuous structures do not exists on the obtained materials, just an association of HAp rod-like nanoparticles, meaning that during the material formation the

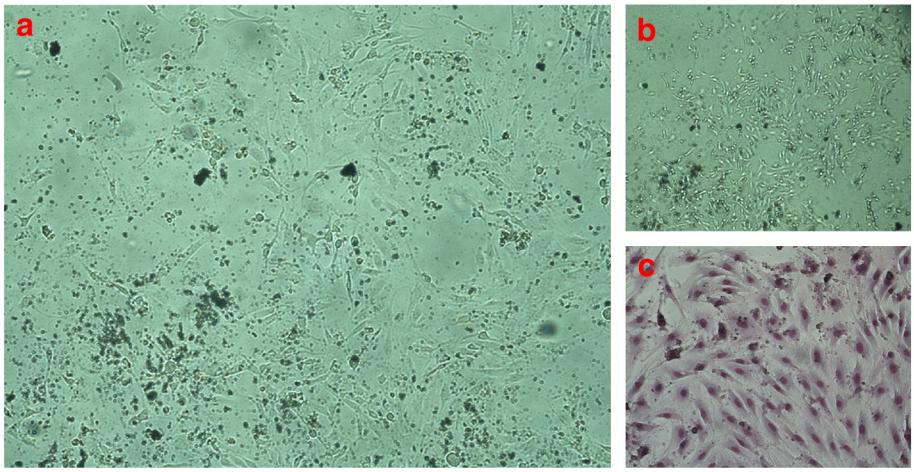

Fig. 9. Effects of material on rat calvarian osteoblast adhesion and morphology; T2 after 72 h of treatment. Hydroxyapatite crystals are seen as dark spots, while the cells are translucent and refractive bodies. (a) Microscopic observation at 20× and (b) 4× magnifications; (c) cell morphology after Giemsa stain.

polymer mineralization did not take place. However there is a change in the Ca/P ratio of the material and surface morphology due to the polymer presence and its specific adsorption on micellar aggregates. Such fact alters the distance between HAp nano-rods and consequently the micro-rough and porosity of the material.

The role of material surface texture was revealed as a key factor in their in vitro bioactivity properties. The bioactivity of the materials was analyzed based on the method developed by Kokubo et al. We found that the topography of each surface follows a direct relationship with the micro-morphology, chemical composition and kinetic growth of the mineral Ca-P coating. On rough surfaces, the valleys seem to be the preferential sites for the nucleation and growth of calcium phosphates. After bioactivity assay, MIII and MIV materials with skewness parameter $R_{sk} > 2.62$ favored the formation of net-like phase on its surfaces with a total Ca/P ratio of about 1. In contrast, MI and MII ($R_{sk} \leq 2.62$) induced the appearance of spherulitic-like structures and a final Ca/P ratio very similar to those existing in trabecular bone (≈ 1.53).

Net-like coating presents the highest value of growth kinetic constant with $n < 1$; while for the spherulitic phase's coating growth, the Avrami constant is 1.75 inferior and the reaction order is superior to the unity. Taking into account that the surface heterogeneity topographies of MI, MII, MIII and MIV materials have significant differences; the acceleration of the nucleation of the apatite over the materials is attributed to the surface topographical changes at the micrometer level. The different patterns of growth occur by means of the matching of the structure of crystal planes in the material and the apatite layer formed. The materials' biocompatibility, confirmed by osteoblast viability and cellular adhesion tests, is a significant indicator of their potential abilities to induce the desired cellular response, favoring integration into the host tissue and stimulating self-healing processes that are the focus of our current research.

The creation of implantable devices with a specific bioactive characteristic may be useful to manipulate the attachment of cells on mineral coating directly affecting the stability and life of the implant.

Acknowledgements

The authors acknowledge the Universidad Nacional del Sur (PGI 24/ZQ07), the Concejo Nacional de Investigaciones Científicas y Técnicas de la República Argentina (CONICET, PIP-11220100100072), and the Xunta de Galicia (Project 10PXIB206258PR). NLD, ANG and JAL have doctoral fellowships with CONICET. GES and PVM are independent and adjunct researchers of CONICET.

Appendix A. Supplementary material

Material synthesis conditions: hydrothermal treatment effect on materials (TEM characterization); calcination effect on materials (characterization by XRD); polymer concentration effect on materials (TEM characterization); nano-rod size distribution histograms and material composition (Ca/P ratio, EDX characterization). Bioactivity and biocompatibility assays: coating growth, Ca/P ratio and rat calvarial osteoblast viability after 48 and 72 h under control and material treatment conditions. Supplementary data to this article can be found online at http://dx.doi.org/10.1016/j.bbagen.2013.07.020.

References

[1] H. Zhou, J. Lee, Nanoscale hydroxyapatite particles for bone tissue engineering, Acta Biomater. 7 (2011) 2769–2781.
[2] M. Bongio, J.J.J.P. van den Beucken, S.C.G. Leeuwenburgh, J.A. Jansen, Development of bone substitute materials: from 'biocompatible' to 'instructive', J. Mater. Chem. 20 (2010) 8747–8759.
[3] S.V. Dorozhkin, M. Epple, Biological and medical significance of calcium phosphates, Angew. Chem. Int. Ed. 41 (2002) 3130–3146.
[4] R.Z. Le Geros, Properties of osteoconductive biomaterials: calcium phosphates, Clin Orthop Relat Res, vol. 395, 2002, pp. 81–98.
[5] Y. Wang, S. Zhang, K. Wei, N. Zhao, J. Chen, X. Wang, Hydrothermal synthesis of hydroxyapatite nanopowders using cationic surfactant as a template, Mater. Lett. 60 (2006) 1484–1487.
[6] O.C. Wilson, Surface modification of hydroxyapatite: a review, Advances in Biomedical and Biomimetic Materials, John Wiley & Sons, Inc., 2009, pp. 171–181.
[7] L. Borum-Nicholas, O.C. Wilson Jr., Surface modification of hydroxyapatite. Part I. Dodecyl alcohol, Biomaterials 24 (2003) 3671–3679.
[8] O.C. Wilson Jr., J.R. Hull, Surface modification of nanophase hydroxyapatite with chitosan, Mater. Sci. Eng. C 28 (2008) 434–437.
[9] S. Dasgupta, A. Bandyopadhyay, S. Bose, Reverse micelle-mediated synthesis of calcium phosphate nanocarriers for controlled release of bovine serum albumin, Acta Biomater. 5 (2009) 3112–3121.
[10] I. Bauer, S.-P. Li, Y.-C. Han, L. Yuan, M.-Z. Yin, Internalization of hydroxyapatite nanoparticles in liver cancer cells, J. Mater. Sci. Mater. Med. 19 (2008) 1091–1095.
[11] H. Ong, J.C. Loo, F.C. Boey, S. Russell, J. Ma, K.-W. Peng, Exploiting the high-affinity phosphonate–hydroxyapatite nanoparticle interaction for delivery of radiation and drugs, J. Nanopart. Res. 10 (2008) 141–150.
[12] B. Palazzo, M. Iafisco, M. Laforgia, N. Margiotta, G. Natile, C.L. Bianchi, D. Walsh, S. Mann, N. Roveri, Biomimetic hydroxyapatite—drug nanocrystals as potential bone substitutes with antitumor drug delivery properties, Adv. Funct. Mater. 17 (2007) 2180–2188.
[13] S.P. Victor, T.S.S. Kumar, Tailoring calcium-deficient hydroxyapatite nanocarriers for enhanced release of antibiotics, J. Biomed. Nanotechnol. 4 (2008) 203–209.
[14] S. Dorozhkin, Nanodimensional and nanocrystalline apatites and other calcium orthophosphates in biomedical engineering, biology and medicine, Materials, vol. 2, 2009, pp. 1975–2045.
[15] A. Lak, M. Mazloumi, M. Mohajerani, A. Kajbafvala, S. Zanganeh, H. Arami, S.K. Sadrnezhaad, Self-assembly of dandelion-like hydroxyapatite nanostructures via hydrothermal method, J. Am. Ceram. Soc. 91 (2008) 3292–3297.
[16] M.-G. Ma, J.-F. Zhu, Solvothermal synthesis and characterization of hierarchically nanostructured hydroxyapatite hollow spheres, Eur. J. Inorg. Chem. 2009 (2009) 5522–5526.
[17] A.S. Maiolo, M.N. Amado, J.S. Gonzalez, V.A. Alvarez, Development and characterization of poly(vinyl alcohol) based hydrogels for potential use as an articular cartilage replacement, Mater. Sci. Eng. C 32 (2012) 1490–1495.
[18] R. Xin, F. Ren, Y. Leng, Synthesis and characterization of nano-crystalline calcium phosphates with EDTA-assisted hydrothermal method, Mater. Des. 31 (2010) 1691–1694.
[19] R. Xie, Z. Feng, S. Li, B. Xu, EDTA-assisted self-assembly of fluoride-substituted hydroxyapatite coating on enamel substrate, Cryst. Growth Des. 11 (2011) 5206–5214.
[20] S.-H. Yu, H. Colfen, Bio-inspired crystal morphogenesis by hydrophilic polymers, J. Mater. Chem. 14 (2004) 2124–2147.
[21] T. Imae, S. Ikeda, Sphere-rod transition of micelles of tetradecyltrimethylammonium halides in aqueous sodium halide solutions and flexibility and entanglement of long rodlike micelles, J. Phys. Chem. 90 (1986) 5216–5223.
[22] Y. Liu, W. Wang, Y. Zhan, C. Zheng, G. Wang, A simple route to hydroxyapatite nanofibers, Mater. Lett. 56 (2002) 496–501.
[23] R.J.P. Corriu, F. Embert, Y. Guari, A. Mehdi, C. Reye, A simple route to organic–inorganic hybrid materials containing Eu complexes, Chem. Commun. (2001) 1116–1117.
[24] J. Brown, R. Richer, L. Mercier, One-step synthesis of high capacity mesoporous Hg2+ adsorbents by non-ionic surfactant assembly, Microporous Mesoporous Mater. 37 (2000) 41–48.
[25] N. Ibaseta, B. Biscans, Fractal dimension of fumed silica: comparison of light scattering and electron microscope methods, Powder Technol. 203 (2010) 206–210.
[26] S.K. Padmanabhan, A. Balakrishnan, M.-C. Chu, Y.J. Lee, T.N. Kim, S.-J. Cho, Sol–gel synthesis and characterization of hydroxyapatite nanorods, Particuology 7 (2009) 466–470.
[27] R.J. Hunter, Zeta Potential in Colloid Science, in: R.H. Ottewill (Ed.), R.R.L. Academic Press, New York, 1981.
[28] T. Kokubo, H. Kushitani, S. Sakka, T. Kisugi, T. Yamamuro, Solutions able to reproduce in vivo surface-structure changes in bioactive glass-ceramic A-W3, J. Biomed. Mater. Res. 24 (1990) 721–734.
[29] P. Scodelaro Bilbao, R. Boland, A. Russo de Boland, G. Santillán, Arch. Biochem. Biophys. 466 (2007) 15–23.
[30] G.W. Snedecor, W.G. Cochran, Statistical Methods, sixth ed. Iowa State University Press, Iowa, Ames, 1967.
[31] G. Giemsa, Eine vereinfachung und vervollkommnung meiner methylenazur-methlyenblau-eosin-farbemethode zur erzielung der RomanowskyNocht'schen chromatinfarbung, Zentabl. Bakteriol. Parasitenkd. Infectkrankh 37 (1904) 308.
[32] J.M. Coelho, J.A. Moreira, A. Almeida, F.J. Monteiro, Synthesis and characterization of HAp nanorods from a cationic surfactant template method, J. Mater. Sci. Mater. Med. 21 (2010) 2543–2549.
[33] A. Zhu, Y. Lu, Y. Si, S. Dai, Frabicating hydroxyapatite nanorods using a biomacromolecule template, Appl. Surf. Sci. 257 (2011) 3174–3179.
[34] E.S. Gadelmawla, M.M. Koura, T.M.A. Maksoud, I.M. Elewa, H.H. Soliman, Roughness parameters, J. Mater. Process. Technol. 123 (2002) 133–145.
[35] N. Hassan, A. Soltero, D. Pozzo, P.V. Messina, J.M. Ruso, Bioinspired templates for the synthesis of silica nanostructures, Soft Matter 8 (2012) 9553–9562.
[36] A. Giorgilli, D. Casati, L. Sironi, L. Galgani, An efficient procedure to compute fractal dimensions by box counting, Phys. Lett. A 115 (1986) 202–206.
[37] K. Foroutan-pour, P. Dutilleul, D.L. Smith, Advances in the implementation of the box-counting method of fractal dimension estimation, Appl. Math. Comput. 105 (1999) 195–210.
[38] S. Bau, O. Witschger, F. Gensdarmes, O. Rastoix, D. Thomas, A TEM-based method as an alternative to the BET method for measuring off-line the specific surface area of nanoaerosols, Powder Technol. 200 (2010) 190–201.

[39] H. Akkari, I. Bhouri, P. Dubois, M.H. Bedoui, On the relations between 2D and 3D fractal dimensions: theoretical approach and clinical application in bone imaging, Math. Model. Nat. Phenom. 3 (2008) 48–75.
[40] S. Ganguly, S. Basu, S. Sikdar, Determination of the aggregate fractal dimensions in colloidal nanofluids, Proceedings of the Institution of Mechanical Engineers, Part N: Journal of Nanoengineering and Nanosystems, 226, 2012, pp. 3–7.
[41] M.L. Sierra, E. Rodenas, CTAB/poly(propylene glycol) mixed micelles: characterization and its properties as a reaction medium, J. Phys. Chem. 97 (1993) 12387–12392.
[42] K. Tasaki, Poly(oxyethylene)—water interactions: a molecular dynamics study, J. Am. Chem. Soc. 118 (1996) 8459–8469.
[43] A. Bigi, E. Boanini, B. Bracci, A. Facchini, S. Panzavolta, F. Segatti, L. Sturba, Nanocrystalline hydroxyapatite coatings on titanium: a new fast biomimetic method, Biomaterials 26 (2005) 4085–4089.
[44] S. Raynaud, E. Champion, D. Bernache-Assollant, Calcium phosphate apatites with variable Ca/P atomic ratio II. Calcination and sintering, Biomaterials 23 (2002) 1073–1080.
[45] Christian Jager, Thea Welzel, W. Meyer-Zaika, M. Epple, A solid-state NMR investigation of the structure of nanocrystalline hydroxyapatite, Magn. Reson. Chem. 44 (2006) 573–580.
[46] M. Fernández-Leyes, V. Verdinelli, N. Hassan, J. Ruso, O. Pieroni, P. Schulz, P. Messina, Biomimetic formation of crystalline bone-like apatite layers on spongy materials templated by bile salts aggregates, J. Mater. Sci. 47 (2012) 2837–2844.
[47] R. Nagarajan, C.-C. Wang, Theory of surfactant aggregation in water/ethylene glycol mixed solvents, Langmuir 16 (2000) 5242–5251.
[48] P. Alexandridis, T. Alan Hatton, Poly(ethylene oxide), poly(propylene oxide), poly(ethylene oxide) block copolymer surfactants in aqueous solutions and at interfaces: thermodynamics, structure, dynamics, and modeling, Colloids Surf., A Physicochem. Eng. Asp. 96 (1995) 1–46.
[49] W. Meier, Structured polymer networks from O/W-microemulsions and liquid crystalline phases, Langmuir 12 (1996) 6341–6345.
[50] R.G. Chaudhuri, S. Sunayana, S. Paria, Wettability of a PTFE surface by cationic-non-ionic surfactant mixtures in the presence of electrolytes, Soft Matter 8 (2012) 5429–5433.
[51] Guillaume Fleury, Guy Schlatter, Cyril Brochon, Christophe Travelet, Alain Lapp, Peter Lindner, G. Hadziioannou, Topological polymer networks with sliding cross-link points: the “sliding gels”. relationship between their molecular structure and the viscoelastic as well as the swelling properties, Macromolecules 40 (2007) 535–543.
[52] G. He, T. Dahl, A. Veis, A. George, Nucleation of apatite crystals in vitro by self-assembled dentin matrix protein 1, Nat. Mater. 2 (2003) 552–558.
[53] M. Uchida, H.-M. Kim, T. Kokubo, S. Fujibayashi, T. Nakamura, Structural dependence of apatite formation on titania gels in a simulated body fluid, J. Biomed. Mater. Res. A 64A (2003) 164–170.
[54] P.S. Vanzillotta, M.S. Sader, I.N. Bastos, G. de Almeida Soares, Improvement of in vitro titanium bioactivity by three different surface treatments, Dent. Mater. 22 (2006) 275–282.
[55] S. Choi, W.L. Murphy, The effect of mineral coating morphology on mesenchymal stem cell attachment and expansion, J. Mater. Chem. 22 (2012) 25288–25295.
[56] T. Kokubo, H. Kushitani, Y. Ebisawa, Apatite formation on bioactive ceramics in body environment, in: O. H., A. H., S. K. (Eds.), Bioceramics, 1, Ishiyaku EuroAmerica, Tokyo, Japan, 1989, pp. 157–162.
[57] J. Wang, P. Layrolle, M. Stigter, K. de Grook, Biomimetic and electrolytic calcium phosphate coatings on titanium alloy: physicochemical characteristics and cell attachment, Biomaterials 25 (2004) 583–592.
[58] W.M. Mullins, C.R. Elsass, An Avrami analysis of the effects of serum proteins and human albumin on calcium hydroxyapatite crystal growth, B. J. Lett. (1992) 326–328.
[59] C.M. Lopatin, V.B. Pizziconi, T.L. Alford, Crystallization kinetics of sol–gel derived hydroxyapatite thin films, J. Mater. Sci. Mater. Med. 12 (2001) 767–773.
[60] X. Liu, K. Lin, J. Chang, Modulation of hydroxyapatite crystals formed from α-tricalcium phosphate by surfactant-free hydrothermal exchange, CrystEngComm 13 (2011) 1959–1965.